TECHNICAL PAPER

CrossMark

Modulation of the atmospheric turbulence coherent structures by mesoscale motions

Eslam Reda Lotfy[1,2] · Sheikh Ahmad Zaki[3] · Zambri Harun[1] (iD)

Abstract
The precise modeling of turbulence is indispensable for weather forecasting and environmental heat-removal and pollution-dispersion assessment. Models rely on correlations derived from field measurements. Unfortunately, the readings are usually contaminated with mesoscale motions which alter turbulence statistics and mislead the characterization of turbulence coherent structures, the drivers of the heat and mass transport process. This article depicts the interference of the mesoscales in turbulence statistics and coherent structure detection. Atmospheric measurements were taken at EKOMAR on the east coast of Malaysia. Two ultrasonic anemometers at heights of 1.7 and 12 m were utilized. Twelve samples from the convective atmospheric boundary layer were analyzed. Spectral and auto-correlation analysis were conducted to assess the weight of the mesoscales relative to the shear coherent structure scales. The structure inclination angle and timescale were calculated for the wind speed signal with and without the mesoscale scales filtered out. It was found that these interfering structures largely shifts the calculated length- and time-scales of the coherent structures. The improper filtration of the signal may delete part of the coherent structures and hence worsen the situation.

Keywords Atmosphere · Turbulence · Coherent structures

Technical Editor: Jader Barbosa Jr.

✉ Zambri Harun
  zambri@ukm.edu.my

1 Faculty of Engineering and Built Environment, Universiti Kebangsaan Malaysia, UKM, 43600 Bangi, Selangor, Malaysia

2 Mechanical Engineering Department, Alexandria University, Alexandria 21544, Egypt

3 Malaysia-Japan International Institute of Technology, Universiti Teknologi Malaysia, 54100 Kuala Lumpur, Malaysia

1 Introduction

The precise characterization of turbulence coherent structures is inevitable for advanced atmospheric flow modeling [1]. The coherent structures hold large share of kinetic energy and contribute high percentage to the momentum, thermal and mass fluxes between the ground and atmosphere [2]. These coherent structures differ from their counterparts in the canonical flat plate boundary layer in both origin and evolution [3, 4]. Moreover, atmospheric flow is distinguished with high Reynolds' numbers that are difficult to attain in wind tunnel laboratories. Portraying this flow is needed to complement the turbulence theory [5].

Atmospheric flow encompasses a hierarchy of coherent structures of different features and length scales [6]. The main coherent structures are the hairpin vortices, the vortex packets, the near-surface streaks and the roll-cell convective structures. The first three structures are associated with shear while the last is mainly a buoyancy artifact and evolves only under convective atmospheric conditions. For a detailed description of these structures, the readers are referred to the literature [7, 8]. The vortex packets appear

in the flat plate boundary layer in a probable length of 1.3δ [9] and maximum length of 5δ [10]. Where δ is the boundary layer height. Assuming a typical value for δ in the atmospheric boundary layer of 100 m, then a tolerable estimate for the vortex packet length scale is ~ 100 m. Near-surface streaks extend in length to few hundreds of meters (~ 500 m) [11] and carry 27% of the turbulent kinetic energy and 31% of the shear stress [12]. The detection and scaling of the structure is held by many methods [13]. Auto-correlation, cross-correlation and spectral analysis of the wind trace are employed to capture the profiles and behaviours of the coherent structures [14, 15].

Many uncertainties are unavoidable in typical atmospheric turbulence field measurements. One of these is the stationarity of the wind speed. The wind component can be contaminated by mesoscale motions, i.e., weather motions of scales between 2 and 2000 km. Mesoscale motions include large roll-cell structures in the convective boundary layer and gravity waves and drainage flows in the stable boundary layer [16]. The challenge to deal with mesoscale structures is that they do not obey the Monin–Obukhov similarity theory and hence alter the calculated fluxes [17]. Besides, the presence of these motions mislead the stability condition identification [18]. Their impact is more pronounced under stable conditions where turbulence fluxes are minimum [16]. These large-scale motions are still poorly characterized [19, 20]. Their types and scales are site-dependent such that their timescales increase with the size of local surface roughness, which reflects on the turbulence signals contaminated by them [18]. The mesoscale motions introduce an extra low-frequency peak to the signal power spectrum. The turbulence and mesoscale peaks are separated by a spectral gap [21]. In addition to the surface topography, the gap timescale is a function of height and thermal stability [16, 22]. The gap timescale increases with height due to liberation from the ground bounding effect. It is lower under stable stratification compared to convective stratification due to motion suppression in stable conditions. Under deep stable conditions, the mesoscales sustain the turbulent motions even beyond the critical Richardson number [20]. The vertical velocity component is slightly altered by the mesoscales [19, 23] which advocates using its standard deviation as a measure for stability [24]. In most of the cases, researchers tend to filter-out these motions by a high-pass filter of an almost fixed cutoff frequency of 0.01 Hz [17].

Few research (e.g., [25]) investigated the impact of the mesoscale motions on turbulence statistics but non, to the best knowledge of the authors, has assessed their modulation of shear coherent structures. In addition, it is not clear if the 0.01 Hz cutoff frequency does not inadvertently omit part of the shear coherent structures [3]. This study aims at

depicting the deviation caused by the mesoscale motions to the atmospheric turbulence coherent structure analysis. This is believed to be a first step towards efficient removal of these motions from turbulence data. The experimental method including site and instrument description, data processing and analysis techniques are discussed in Sect. 2. Section 3 details the length scales of the different coherent structures and the influence of the mesoscales on the auto-correlation analysis of the velocity signals. Additionally, the compliance of the contaminated signals with the similarity theory is tested. Furthermore, The structure inclination angle is compared with the literature. Finally, the conclusions are listed in Sect. 4.

2 Method

2.1 Site and instruments

Measurements were collected at the Marine Ecosystem Research Centre (EKOMAR) ($2°$ $34'42.11''$N, $103°$ $48'21.05''$E) which is an onshore research facility situated on the east coast of Peninsular Malaysia, 22 km northern the city of Mersing. The location on the east coast makes the site attractive for both the wet and dry monsoon measurements as the wind blows from the sea either directly or through a short vegetation cover. The data were captured through two scientific campaigns; C-I: from 19 September 2017 to 1 October 2017 and C-II: from 7 November 2017 to 18 November 2017. During C-I the wind blew mainly from the south-east direction at an average speed of 2.8 m/s, temperature of 25.7 °C and relative humidity of 76% (read at Mersing weather station), whereas during C-II the wind blew from the north-east direction at an average speed of 2 m/s, temperature of 28 °C and relative humidity of 83%. Two 3D ultrasonic anemometers were used; one CSAT-3B anemometer (Campbell Scientific, USA; 0.001 m/s & 0.002 °C resolution and $\pm$ 0.08 m/s accuracy) and one YOUNG 81000 anemometer (R.M. YOUNG, USA; 0.01 m/s & 0.01°C resolution and $\pm$ 0.05 m/s & $\pm$ 2 °C accuracy) at 1.7 and 12 m heights, respectively. The CSAT-3B anemometer was connected to the PC through a CR1000 data logger (Campbell Scientific, USA), whereas the YOUNG 81000 anemometer was directly connected to the PC. Both anemometers were calibrated in the UKM low speed wind tunnel [26] before the experiment and an error of less than 2% was achieved. The sonic temperature can be set equal to the virtual potential temperature with a minimal error [27–29]. The term temperature will be used to refer to the virtual potential temperature hereafter. In C-I, the wind direction considered is the southeast direction. The wind blowing from this direction comes from the sea and passes over a vegetation cover (tropical forest) of 10–

15 m height and $\sim$1 km stretch. The instruments lie 200 m downwind the vegetation cover and surrounded from all other direction (within a > 20 m circle) by tropical forests except from the north side where the seashore extends. The forest is interspersed by few Malaysian-style houses. In C-II the wind blows directly from the sea. The ground topography is plain and covered with 5–10 cm grass. Satellite and aerial pictures for the site and pictures for the wind blowing directions are illustrated in Fig. 1. The sampling rate was set to 20 Hz and data were divided into samples of time-lengths 42 min in C-I and 30 min in C-II,

this is thought to be enough for turbulence statistics to converge [2, 5, 30].

2.2 Data screening

The first step in data analysis is to determine the mean wind direction (α) over each sampling interval and convert the velocity readings from the instrument coordinates (u_{inst} and v_{inst}) to a coordinate system based on the mean wind direction (u and v) [3]. These are summarized in the following equations:

Fig. 1 Site illustration. **a** A satellite photo of the EKOMAR site. **b** A picture towards the wind blowing direction in C-I. **c** An aerial photo for the site. (d) A picture towards the wind blowing direction in C-II

$$\alpha = \tan^{-1}\left(\frac{V_{inst}}{U_{inst}}\right) \tag{1}$$

$$u = u_{inst}\cos(\alpha) + v_{inst}\sin(\alpha) \tag{2}$$

$$v = v_{inst}\cos(\alpha) - u_{inst}\sin(\alpha) \tag{3}$$

where, the small letters refer to the instantaneous velocities and the capital letters to the time-mean velocities.

At this time of the year during the transition from the dry to the wet monsoons, the wind blows over Malaysia from different directions along the day. In addition, the location near the sea makes the wind direction vulnerable to change with height owing to the sea and land breezes. The screening criterion was to admit only the data of wind blowing from the correct direction (112-162° in C-I and -4° to 14° or 36° to 54° in C-II) with a difference in angle between the bottom and top levels within ±15° in C-I and ±9° in C-II. Finally, a total of 13 samples (12 convective cases and one stable case) in C-I and 48 convective samples in C-II were ready for processing. Due to the scarcity of valid stable data, the research was focused on convective atmosphere. The coherent wind structures or mesoscale motions due to the nonstationarity of the weather are characterized with very large scales which can go streamwise as far as several kilometers. Consequently, these structures can be excluded by subjecting the data to a high-pass filter [25, 31]. Few techniques have been devised to preclude the mesoscale motions from velocity and temperature signals [16, 18]. These depend mainly on identifying the spectral gap between turbulence motions and mesoscales. Figure 2 represents the spectra of the windward velocity (u) for selected cases in C-I covering the range of stability analyzed. The mesoscales introduce peak-

Fig. 2 Power spectra of the u signal at different stability conditions represented by different values of ζ. Data correspond to C-I. The lines are moving-average fittings for the data

energies at low frequencies [32]. The optimum cutoff frequency which achieves the compromise between turbulence coherent structures and mesoscales is defined as the intermediate trough between the peaks of the two motions. As displayed, this trough changes from one case to another, as expected by [18]. However, a reasonable edge for the current dataset is 0.0035 Hz. Hence, a conservative cutoff frequency maybe taken as 0.0025 Hz. The popular cutoff frequency of 0.01 Hz [17] erodes the near-surface streaks. The 0.0025 Hz cutoff frequency corresponds to a $\sim$750-m Taylor length-scale. This 0.0025 Hz cutoff frequency compares with the gap scale predicted by Conangla et al. [22]. It is important to stress that we do not adopt a certain value for the cutoff frequency but rather argue the need to visit the power spectrum of the signal to determine the optimum cutoff frequency. Applying the same method to C-II data, a 0.0075 Hz frequency was assigned for the partitioning. The increase in frequency (decrease in time-scale) was expected as the mesoscales show lower time-scales over flat surfaces. Throughout this research, unless otherwise mentioned, the C-I campaign is the default source of the results. Figure 3 shows an example of fluctuating velocity trace before and after filtration.

2.3 Analysis

The thermal stratification estimator adopted in the current research is the Obukhov stability parameter (ζ), defined as:

$$\zeta = \frac{z}{L} = \frac{z\kappa g\theta^*}{u^{*2}\Theta} \tag{4}$$

Where L is the Obukhov length, z is the height above ground level, κ is the Von Karman constant taken here as 0.41, g is the gravitational acceleration (9.81 m/s²), U and Θ are the time mean wind speed and temperature, and u^* and θ^* are the friction velocity and friction temperature. The friction velocity and temperature were calculated from the momentum and heat fluxes as follows:

$$u^* = \sqrt{-\overline{u'w'}}, \theta^* = -\frac{\overline{w'\theta'}}{u^*} \tag{5}$$

u^*, θ^* and ζ were obtained from the near-ground anemometer (1.7 m) while the mean windward velocity, the length scales, and wind direction were obtained from the 12-m anemometer. A summary of the mean wind speeds and directions, friction velocities and stability conditions of the collected samples for both the contaminated and filtered signals is shown in Table 1.

The dimensionless wind shear (ϕ_M) and thermal stratification (ϕ_H) were used to assess the effect of the mesoscale structures on the validity of the Monin–Obukhov similarity theory. They are given by:
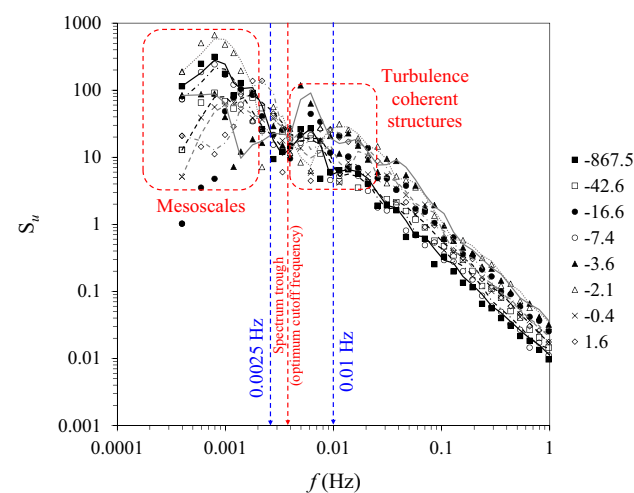
Fig. 3 Traces of fluctuating velocity components; **a** the raw signal, **b** the removed mesoscale signal and **c** the filtered signal. The data correspond to the sample collected on 22/9/2017 4:34 PM by the 12-m anemometer
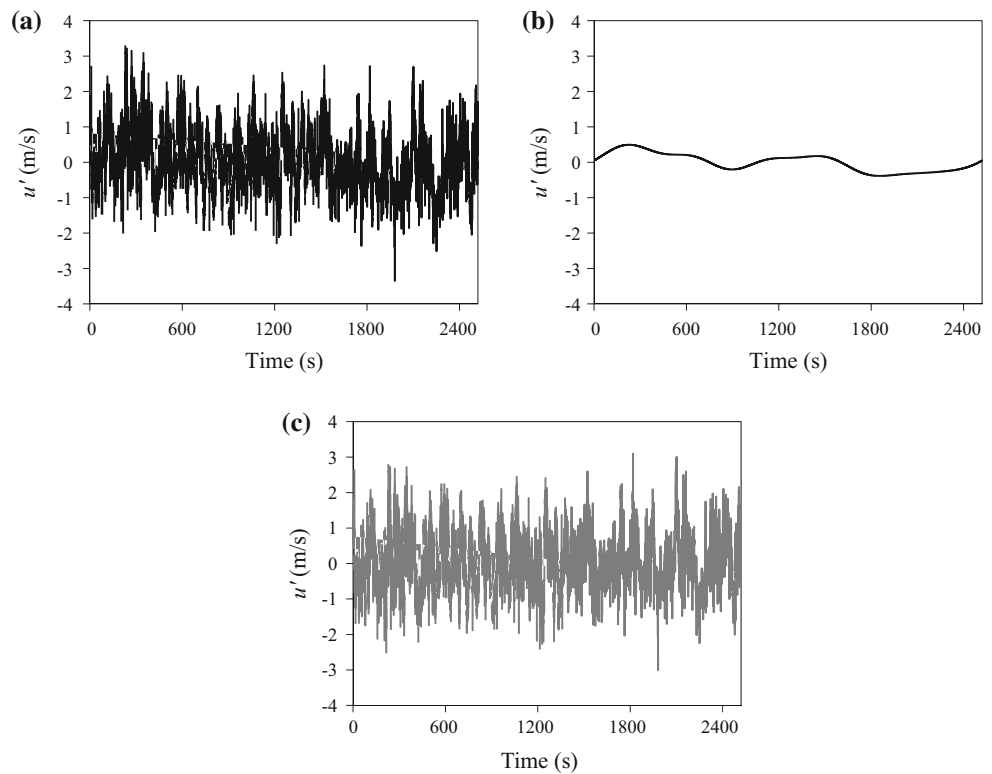
Table 1 A summary of the wind conditions for the collected samples

Date and time	U (m/s)	Wind direction	$u*$		ζ	
			Original signal	Filtered signal	Original signal	Filtered signal
22/9/17 4:34 PM	1.59	141	0.094	0.088	− 6.4	− 7.9
22/9/17 5:16 PM	1.71	151	0.093	0.088	− 4.6	− 6.1
23/9/17 10:34 AM	2.13	125	0.078	0.095	− 33.6	− 18.0
23/9/17 11:16 AM	1.82	125	0.105	0.069	− 12.0	− 42.6
24/9/17 4:34 PM	2.38	126	0.098	0.034	− 5.6	− 140.8
24/9/17 5:16 PM	2.07	143	0.113	0.106	− 3.1	− 3.6
25/9/17 10:34 AM	1.99	139	0.193	0.168	− 1.8	− 2.9
25/9/17 11:16 AM	2.19	132	0.103	0.104	− 17.6	− 16.6
25/9/17 4:34 PM	2.71	117	0.094	0.093	− 0.9	− 2.1
25/9/17 5:16 PM	1.87	136	0.136	0.127	− 0.4	− 0.4
26/9/17 5:16 PM	1.45	118	0.137	0.090	− 2.2	− 7.4
29/9/17 11:16 AM	0.91	146	0.083	0.023	− 18.1	− 867.5

$$\phi_M = \frac{\kappa z}{u^*}\frac{\partial U}{\partial z}, \quad \phi_H = \frac{\kappa z}{\theta^*}\frac{\partial \Theta}{\partial z} \quad (6)$$

These parameters were correlated by Dyer [33] in the form:

For the **stable** surface layer ($\zeta > 0$):

$$\phi_M = \phi_H = 1 + 5\zeta \quad (7)$$

For the **convective** surface layer ($\zeta < 0$):

$$\phi_M = (1 - 16\zeta)^{-1/4} \quad (8)$$

$$\phi_H = (1 - 16\zeta)^{-1/2} \quad (9)$$

The turbulence coherent structure (vortex packet) inclination angle (γ) was computed from cross-correlation analysis between the lower and higher anemometer u'-signals. The cross-correlation yields the time-lag between the two signals which can be converted to a streamwise distance by applying the Taylor's frozen turbulence hypothesis. viz,

$$\Delta x^* = U_{1.7m} \times \text{Time} - \text{lag} \quad (10)$$

Dennis and Nickels [34] proved the applicability of the hypothesis for projection distances up to 6δ. The inclination angle can be calculated then from:

$$\tan(\gamma) = \frac{\Delta z}{\Delta x^*} \qquad (11)$$

where, Δz is the height difference between the two sensors, namely 10.3 m. Each 42 min sample was subdivided into 6-min intervals ($\sim 1/0.0025$ Hz) to concentrate the cross-correlation on 6-12 vortex packets only. Refer to [35] for a review on coherent structure timescale. Then the inclination angle of the sample was estimated as an average over all the intervals.

On the other hand, turbulence coherent structures were detected via the u-level algorithm [30, 35–37]. According to the algorithm, any structure having a fluctuating velocity less than a certain threshold was recognized as a coherent structure. A negative unity standard deviation threshold ($-\sigma_u$) was utilized. Högström and Bergström [35] examined various threshold values and found a slight change in the calculated packet time in the range $-0.2\sigma_u \rightarrow -1.1\sigma_u$. Högström and Bergström reported also that hairpins separated by less than ~ 1.75 seconds belong to the same vortex packet. Hence, in this research hairpins separated by less than this interval were combined in a single vortex packet. The vortex packet timescale is defined as the total sample time divided by the number of detected structures. Afterward, the relative contributions of the detected coherent structures to the total turbulent kinetic energy and mass and heat fluxes were calculated following Barthlott et al. [38], as:

$$C_{u'u'} = \frac{\sum u'^2_{\text{coh}}}{\sum u'^2_{\text{sample}}} \qquad (12)$$

$$C_{u'w'} = \frac{\sum u'w'_{\text{coh}}}{\sum u'w'_{\text{sample}}} \qquad (13)$$

$$C_{w'\theta'} = \frac{\sum u'\theta'_{\text{coh}}}{\sum u'\theta'_{\text{sample}}} \qquad (14)$$

In the inclination angle and structure detection analysis, a low-pass filter (1 Hz) was applied to remove the interference from the instrument internal noise and smooth the signal and hence facilitate structure detection [38].

3 Results and discussion

3.1 Length scales

The length scales cut by the filter are illustrated by the spectral analysis of the velocity components and temperature, Fig. 4. The figure shows the average spectra for all

samples measured by the 12 m anemometer. The length scale was calculated as $\lambda_x = nU$; where n is the frequency and U is the average wind speed. It is clear in all graphs, except the w component, the bi-modal behavior discovered originally by Kim and Adrian [39] and confirmed later on by many authors in both the flat plate [15, 40] and the atmospheric boundary layers [4, 5]. The two modes correspond to the vortex packets (~ 100 m) and the surface streaks (~ 400 m). Surprisingly, the w-spectrum, Fig. 4c, receives little contribution from either the mesoscale motions or surface streaks. The averaged auto-correlations of the u' and w' signals are illustrated in Fig. 5. The deepest trough of the curve defines the length of the dominant structure since it represents the time lag at which the shifted structure tail (velocity increase) matches its head (velocity decrease) in the original signal Fig. 5c. The length scales of the unfiltered signals are shifted towards the mesoscales in case of the u' trace, Fig. 5a. But for w', Fig. 5b, the auto-correlation function coincides for both the filtered and unfiltered signals which agrees with the spectral analysis. It is worth mentioning that the correlation becomes sharper (absolute coefficient is higher) after filtering out the mesoscale motions.

A comprehensive picture about the existing mesoscale motions can now be drawn. The motions presented in the current research comprise of horizontal waves, i.e., variations in u and v components due to interaction between two wind sources; one is hot and the other is cold. The coefficients of correlation between the filtered signals of u, v, w and θ are listed in Table 2. The correlation coefficient between the windward and cross-wind signals is null which is a natural feature of a $u - v$ wave. w correlates by comparable coefficients with both u and v. Nevertheless, Its correlation with θ is too weak which asserts the mechanical origin of the w modulation. A spectral analysis of the single stable case (not shown) illustrate the presence of these horizontal waves even under stable conditions.

3.2 Compliance with the similarity theory

A comparison between the turbulence statistics and dimensionless parameters for both the filtered and unfiltered signals, Fig. 6, reveals a noticeable scatter in the unfiltered signals. The analysis is based on the C-II campaign since it provides more data for comparison with the empirical correlations. For the normalized velocity fluctuations, Fig. 6a, the filtered data approach values of 2.8, 2.3 and 1.42 for u, v and w at neutral stratification which are quite in agreement with those of Panofsky et al. [41] (2, 2 and 1.26) and Wyngaard and Coté [42] (2.3, 2.3 and 1.3), respectively. Meanwhile, the unfiltered signals approach 3.4, 2.77 and 1.41, respectively. On the other hand, for the dimensionless parameters, shown in Fig. 6b, in addition to

Fig. 4 Spectral analysis of **a** u', **b** v', **c** w' and **d** θ'. Continuous lines indicate filtered signals and diamond markers indicate unfiltered signals
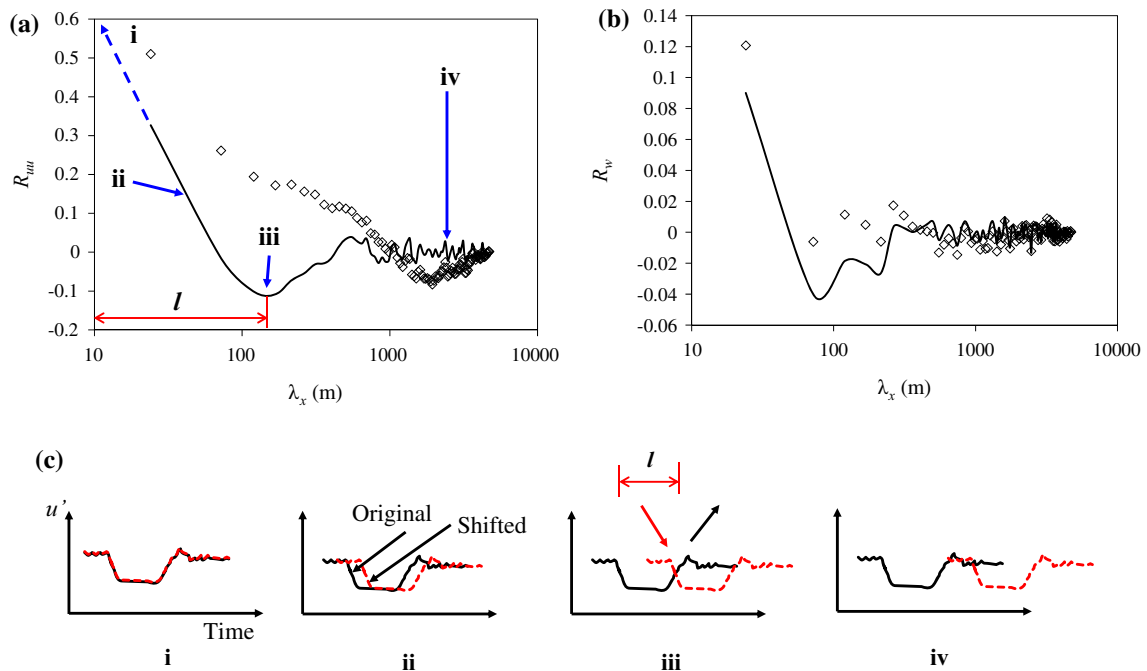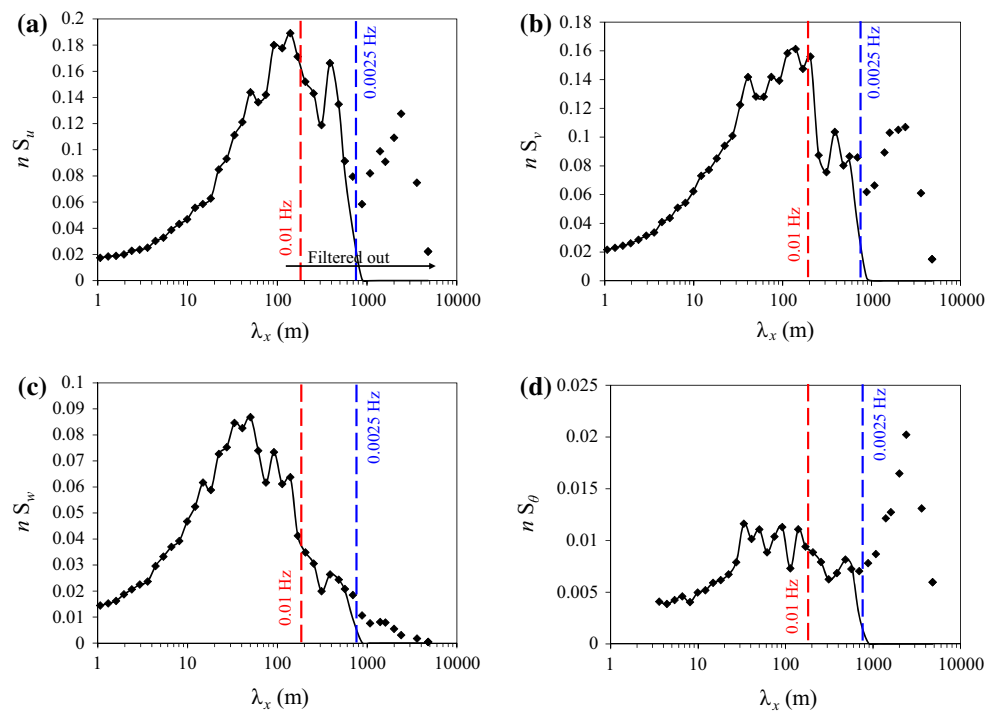

Fig. 5 Auto-correlation analysis for the **a** u' and **b** w' components. Continuous lines indicate filtered signals and diamond markers indicate unfiltered signals. (c) displays the basis for estimating the structure length from auto-correlation analysis; the continuous line represents the original signal and the dashed line represents the shifted signal. (i) A zero shift between the two signals produces the maximum correlation (unity), (ii) as the shift increases, the correlation weakens, (iii) the structure extent (l) emerges at the trough when the head of the structure in the original signal coincides with its tail in the shifted signal, (iv) the correlation coefficient fluctuates around zero after totally passing the turbulence coherent structure

Table 2 Coefficients of correlation between the filtered signals. The data correspond to the sample collected on 22/9/2017 4:34 PM by the 12 m anemometer

	$u - v$	$v - w$	$w - u$	$\theta - u$	$\theta - v$	$\theta - w$
Coefficients	0.076	0.4	0.24	-0.8	0.15	-0.03

the obvious deviation, the sum of square deviations from Dyer correlations ($\zeta < 0$) is higher in case of the contaminated signals. This is in as much as the mesoscale motions do not obey the Monin–Obukhov similarity theory.

3.3 Turbulence coherent structures

As has been deduced from the auto-correlation analysis in Sect. 3.1, the calculation of the length scale of the near-surface streaks is thoroughly misled by the mesoscale motions. Now we are to test the modulating effect of these motions on the vortex packet inclination angle (γ). A comparison between the unfiltered data, data filtered at 0.0025 Hz, data filtered at 0.01 Hz and data from the literature is illustrated in Fig. 7. The mesoscale motions apply little distortion to the inclination angles. However, the angles derived from data subjected to the 0.01 Hz filter attain more scattered values. This indicates weaker cross-correlation between the two series, i.e., some vortex packets are missing in the higher frequency filtered data. This is the 0.01 Hz filter partitions part of the turbulence coherent structures. Before leaving the discussions on inclination angle, it is worth illustrating the significance of the 6-min averaging period employed. As can be noticed in
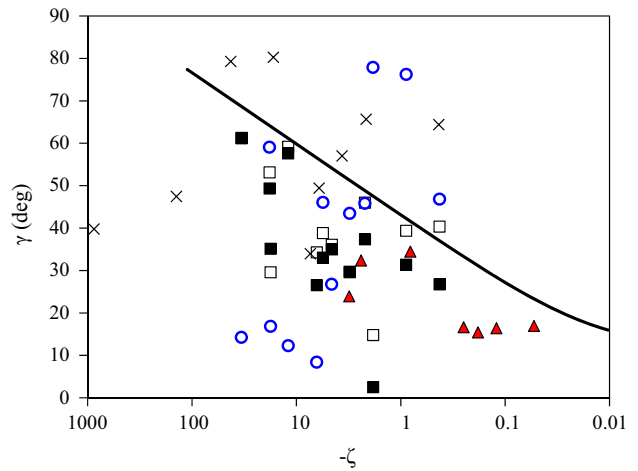
Fig. 7 Variation of the vortex packet inclination angle under convective atmospheric conditions. Dark squares: unfiltered data, open squares: data filtered at 0.0025 Hz, circles: data filtered at 0.01 Hz, continuous line: [1], triangles: [43], crosses: data filtered at 0.0025 Hz and 42-min correlation period

Fig. 7, applying the cross-correlation to the whole 42 min introduces scatters to the calculated angle, though within the expected range. Hence, the convergence of the angle requires more data than what is currently available. Table 3 displays average values of the calculated structure time scale and participation to the total flux for the unfiltered and two filtered cases. The values correspond to the 12-m anemometer signals. It is clear that the mesoscales slightly harm the calculations of the coherent structure statistics. These large structures modulate the signal such that the standard deviation of the unfiltered signal (the threshold of the detection algorithm) is higher and hence fewer structures can fulfill the detection criterion. This interprets the
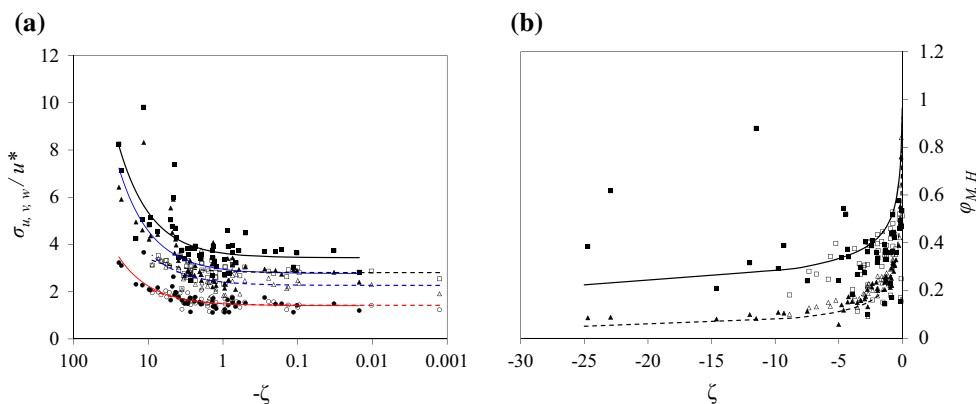
Fig. 6 Examining the compliance with the Monin–Obukhov similarity theory at convective conditions. **a** Turbulence fluctuations. Squares: σ_u/u^*, triangles: σ_v/u^*, circles: σ_w/u^*. Continuous and dashed lines are linear fittings for the unfiltered and filtered σ_u/u^*, σ_v/u^* and σ_w/u^*. **b** Dimensionless shear and thermal stratification.

Squares: ϕ_M, triangles: ϕ_H. Continuous and dashed lines represent Dyer [33] correlations for ϕ_M and ϕ_H, respectively. Dark symbols refer to the unfiltered signals and open symbols to the filtered ones. Based on the C-II campaign dataset

Table 3 Coherent structure timing and contributions to the total momentum and heat fluxes for the unfiltered and the two filtered signals

	T_s (%)	$C_{u'u'}$ (%)	$C_{u'w'}$ (%)	$C_{w'\theta'}$ (%)	t_p (s)
Unfiltered data	19	36	31	25	29
Data filtered at 0.0025 Hz	19	37	33	25	22
Data filtered at 0.01 Hz	18	39	38	34	17

T_s: percentage of the total sample duration occupied by structures

$C_{u'u'}$: structure contribution to $\overline{u'^2}$

$C_{u'w'}$: structure contribution to $\overline{u'w'}$

$C_{w'\theta'}$: structure contribution to $\overline{w'\theta'}$

t_p: single packet time

larger time-per-structure (t_p) and smaller energy and flux contributions ($C_{u'u'}$, $C_{u'w'}$ and $C_{w'\theta'}$) gained from the mesoscale altered signals.

4 Conclusions

The modulation imposed by the mesoscale motions on the turbulence coherent structures was examined in this research. Atmospheric flow data were collected at an onshore scientific facility for two weeks. Two ultrasonic anemometers at 1.7 m and 12 m levels above ground were set up in the study. Data screening produced twelve 42-min samples covering a wide range of convective atmospheric conditions. The conclusions of the analysis are:

– The mesoscale motions show comparable or higher energies to those of the shear coherent structures. The only exception is the vertical velocity component where their role in the spectra diminishes.
– The length scales calculated from the auto-correlation analysis are shifted towards these large scales except for the vertical velocity.
– The mesoscale motions imply scatter of turbulence statistics since these structures disobey the similarity theory.
– The common cutoff frequency (0.01 Hz) used to remove the mesoscale motions partitions a considerable portion of the shear coherent structures and hence underestimates or overestimates the structure inclination angle.
– The modulating effect of the mesoscale motions raises the standard deviation of the velocity trace which handicaps the realization of the coherent structures. Thus, fewer and shorter structures are detected in a contaminated signal.

In conclusion, more research is needed with sufficient number of data to quantify the modulating effect of the mesoscale motions on the turbulence coherent structure analysis and to devise techniques to separate them without harming the large scale shear motions.

References

1. Chauhan K, Hutchins N, Monty J, Marusic I (2013) Structure inclination angles in the convective atmospheric surface layer. Bound-Layer Meteorol 147:1–10. https://doi.org/10.1007/s10546-012-9777-7
2. Serafimovich A, Thomas C, Foken T (2011) Vertical and horizontal transport of energy and matter by coherent motions in a tall spruce canopy. Bound-Layer Meteorol 140(3):429–451. https://doi.org/10.1007/s10546-011-9619-z
3. Hutchins N, Chauhan K, Marusic I, Monty J, Klewicki J (2012) Towards reconciling the large-scale structure of turbulent boundary layers in the atmosphere and laboratory. Bound-Layer Meteorol 145(2):273–306
4. Guala M, Metzger M, McKeon B (2011) Interactions within the turbulent boundary layer at high Reynolds number. J Fluid Mech 666:573–604. https://doi.org/10.1017/s0022112010004544
5. Kunkel GJ, Marusic I (2006) Study of the near-wall-turbulent region of the high-Reynolds-number boundary layer using an atmospheric flow. J Fluid Mech 548:375–402. https://doi.org/10.1017/s0022112005007780
6. Salesky ST, Chamecki M, Bou-Zeid E (2017) On the nature of the transition between roll and cellular organization in the convective boundary layer. Bound-Layer Meteorol 163(1):41–68. https://doi.org/10.1007/s10546-016-0220-3
7. Dennis DJ (2015) Coherent structures in wall-bounded turbulence. An Acad Bras Ciênc 87(2):1161–1193. https://doi.org/10.1590/0001-3765201520140622
8. Young GS, Kristovich DA, Hjelmfelt MR, Foster RC (2002) Supplement to rolls, streets, waves, and more. Bull Am Meteorol Soc 83(7):1001–1001. https://doi.org/10.1175/bams-83-7-young
9. Adrian RJ, Meinhart CD, Tomkins CD (2000) Vortex organization in the outer region of the turbulent boundary layer. J Fluid Mech 422:1–54. https://doi.org/10.1017/s0022112000001580
10. Dennis DJ, Nickels TB (2011) Experimental measurement of large-scale three-dimensional structures in a turbulent boundary layer. J Fluid Mech 673:180–217. https://doi.org/10.1017/s0022112010006324

11. Träumner K, Damian T, Stawiarski C, Wieser A (2015) Turbulent structures and coherence in the atmospheric surface layer. Bound-Layer Meteorol 154(1):1–25. https://doi.org/10.1007/s10546-014-9967-6

12. Fang J, Porté-Agel F (2015) Large-eddy simulation of very-large-scale motions in the neutrally stratified atmospheric boundary layer. Bound-Layer Meteorol 155(3):397–416. https://doi.org/10.1007/s10546-015-0006-z

13. Alfonsi G (2006) Coherent structures of turbulence: methods of eduction and results. Appl Mech Rev 59(6):307–323. https://doi.org/10.1115/1.2345370

14. Ganapathisubramani B, Hutchins N, Hambleton W, Longmire E, Marusic I (2005) Investigation of large-scale coherence in a turbulent boundary layer using two-point correlations. J Fluid Mech 524:57–80. https://doi.org/10.1017/s0022112004002277

15. Hutchins N, Marusic I (2007) Evidence of very long meandering features in the logarithmic region of turbulent boundary layers. J Fluid Mech 579:1–28. https://doi.org/10.1017/s0022112006003946

16. Vickers D, Mahrt L (2003) The cospectral gap and turbulent flux calculations. J Atmos Oceanic Technol 20(5):660–672. https://doi.org/10.1175/1520-0426(2003)20%3c660:tcgatf%3e2.0.co;2

17. Basu S, Porté-Agel F, Foufoula-Georgiou E, Vinuesa J-F, Pahlow M (2006) Revisiting the local scaling hypothesis in stably stratified atmospheric boundary-layer turbulence: an integration of field and laboratory measurements with large-eddy simulations. Bound-Layer Meteorol 119(3):473–500. https://doi.org/10.1007/s10546-005-9036-2

18. Acevedo OC, Costa FD, Oliveira PE, Puhales FS, Degrazia GA, Roberti DR (2014) The influence of submeso processes on stable boundary layer similarity relationships. J Atmos Sci 71(1):207–225. https://doi.org/10.1175/jas-d-13-0131.1

19. Mahrt L (2009) Characteristics of submeso winds in the stable boundary layer. Bound-Layer Meteorol 130(1):1–14. https://doi.org/10.1002/qj.2835

20. Mahrt L (2010) Variability and maintenance of turbulence in the very stable boundary layer. Bound-Layer Meteorol 135(1):1–18. https://doi.org/10.1002/qj.2835

21. Van der Hoven I (1957) Power spectrum of horizontal wind speed in the frequency range from 0.0007 to 900 cycles per hour. J Meteorol 14(2):160–164. https://doi.org/10.1175/1520-0469(1957)014%3c0160:psohws%3e2.0.co;2

22. Conangla L, Cuxart J, Soler M (2008) Characterisation of the nocturnal boundary layer at a site in northern spain. Bound-Layer Meteorol 128(2):255–276. https://doi.org/10.1007/s10546-008-9280-3

23. Vickers D, Mahrt L (2007) Observations of the cross-wind velocity variance in the stable boundary layer. Environ Fluid Mech 7(1):55–71. https://doi.org/10.1007/s10652-006-9010-7

24. Acevedo OC, Moraes OL, Degrazia GA, Fitzjarrald DR, Manzi AO, Campos JG (2009) Is friction velocity the most appropriate scale for correcting nocturnal carbon dioxide fluxes? Agric For Meteorol 149(1):1–10. https://doi.org/10.1016/j.agrformet.2008.06.014

25. Dias NL, Chamecki M, Kan A, Okawa CM (2004) A study of spectra, structure and correlation functions and their implications for the stationarity of surface-layer turbulence. Bound-Layer Meteorol 110(2):165–189. https://doi.org/10.1023/A:1026067224894

26. Harun Z, Ghopa WAW, Abdullah A, Ghazali MI, Abbas AA, Rasani MR, Zulkifli R, Wan Mahmood WMF, Mansor MRA, Abidin ZZ, Wan Mohtar WHM (2016) The development of a multi-purpose wind tunnel. J Teknol 10:63–70 (10.11113)

27. Larsén X, Smedman AS, ögström UH (2004) Air–sea exchange of sensible heat over the baltic sea. Q J Royal Meteorol Soc 130(597):519–539 (10.1256/qj.03.11)

28. Kaimal J, Gaynor J (1991) Another look at sonic thermometry. Bound-Layer Meteorol 56(4):401–410. https://doi.org/10.1007/bf00119215

29. Högström U, Smedman A-S (2004) Accuracy of sonic anemometers: laminar wind-tunnel calibrations compared to atmospheric in situ calibrations against a reference instrument. Bound-Layer Meteorol 111(1):33–54. https://doi.org/10.1023/b:boun.0000011000.05248.47

30. Boppe RS, Neu W (1995) Quasi-coherent structures in the marine atmospheric surface layer. J Geophys Res Oceans 100(C10):20635–20648. https://doi.org/10.1029/95jc02305

31. Kaimal J, Wyngaard J, Haugen D, Coté O, Izumi Y, Caughey S, Readings C (1976) Turbulence structure in the convective boundary layer. J Atmos Sci 33(11):2152–2169. https://doi.org/10.1175/1520-0469(1976)033%3c2152:tsitcb%3e2.0.co;2

32. Cuxart J, Yagüe C, Morales G, Terradellas E, Orbe J, Calvo J, Fernández A, Soler M, Infante C, Buenestado P et al (2000) Stable atmospheric boundary-layer experiment in spain (sables 98): a report. Bound-Layer Meteorol 96(3):337–370. https://doi.org/10.1023/a:1002609509707

33. Dyer A (1974) A review of flux-profile relationships. Bound-Layer Meteorol 7(3):363–372. https://doi.org/10.1007/bf00240838

34. Dennis DJ, Nickels TB (2008) On the limitations of taylor's hypothesis in constructing long structures in a turbulent boundary layer. J Fluid Mech 614:197–206. https://doi.org/10.1017/s0022112008003352

35. Högström U, Bergström H (1996) Organized turbulence structures in the near-neutral atmospheric surface layer. J Atmos Sci 53(17):2452–2464. https://doi.org/10.1175/1520-0469(1996)053%3c2452:otsitn%3e2.0.co;2

36. Lu S, Willmarth W (1973) Measurements of the structure of the Reynolds stress in a turbulent boundary layer. J Fluid Mech 60(3):481–511. https://doi.org/10.1017/s0022112073000315

37. W. G. Tiederman, Eulerian detection of turbulent bursts, Near-Wall Turbulence 874–887 (1990)

38. Barthlott C, Drobinski P, Fesquet C, Dubos T, Pietras C (2007) Long-term study of coherent structures in the atmospheric surface layer. Bound-Layer Meteorol 125(1):1–24. https://doi.org/10.1007/s10546-007-9190-9

39. Kim K, Adrian R (1999) Very large-scale motion in the outer layer. Phys Fluids 11(2):417–422. https://doi.org/10.1063/1.869889

40. Harun Z, Monty JP, Mathis R, Marusic I (2013) Pressure gradient effects on the large-scale structure of turbulent boundary layers. J Fluid Mech 715:477–498. https://doi.org/10.1017/jfm.2012.531

41. Panofsky HA, Tennekes H, Lenschow DH, Wyngaard J (1977) The characteristics of turbulent velocity components in the surface layer under convective conditions. Bound-Layer Meteorol 11(3):355–361. https://doi.org/10.1007/bf02186086

42. Wyngaard JC, Coté O (1974) The evolution of a convective planetary boundary layer higher-order-closure model study. Bound-Layer Meteorol 7(3):289–308

43. Carper MA, Porté-Agel F (2004) The role of coherent structures in subfilter-scale dissipation of turbulence measured in the atmospheric surface layer. J Turbul 5:32. https://doi.org/10.1088/1468-5248/5/1/040